

Modified temperature redshift relation and UHECR propagation

Janning Meinert^{1,2*}, Leonel Morejón^{1†}, Alexander Sandrock^{1‡}, Björn Eichmann^{3§},
Jonas Kreidelmeyer^{4¶}, Karl-Heinz Kampert^{1||}

¹Bergische Universität Wuppertal, Department of Physics, Gaußstraße 20, 42103 Wuppertal, Germany

²Institut für Theoretische Physik, Universität Heidelberg Philosophenweg 12, D-69120 Heidelberg, Germany

³Ruhr-Universität Bochum, Theoretische Physik IV, Fakultät für Physik und Astronomie, Universitätsstraße 150, 44801 Bochum, Germany

⁴Institut für Experimentalphysik, Universität Hamburg, DESY, Luruper Chaussee 149, Hamburg, Germany

A Preprint 2 May 2024

ABSTRACT

We re-examine the interactions of ultra-high energy cosmic rays (UHECRs) with photons from the cosmic microwave background (CMB) under a changed, locally non-linear temperature redshift relation $T(z)$. This changed temperature redshift relation has recently been suggested by the postulate of subjecting thermalised and isotropic photon gases such as the CMB to an SU(2) rather than a U(1) gauge group. This modification of Λ CDM is called SU(2)_{CMB}, and some cosmological parameters obtained by SU(2)_{CMB} seem to be in better agreement with local measurements of the same quantities, in particular H_0 and S_8 . In this work, we apply the reduced CMB photon density under SU(2)_{CMB} to the propagation of UHECRs. This leads to a higher UHECR flux just below the ankle in the cosmic ray spectrum and slightly more cosmogenic neutrinos under otherwise equal conditions for emission and propagation. Most prominently, the proton flux is significantly increased below the ankle (5×10^{18} eV) for hard injection spectra and without considering the effects of magnetic fields. The reduction in CMB photon density also favours a decreased cosmic ray source evolution than the best fit using Λ CDM. In consequence, it seems that SU(2)_{CMB} favours sources that evolve as the star formation rate (SFR), like starburst galaxies (SBG) and gamma-ray bursts (GRB), over active galactic nuclei (AGNs) as origins of UHECRs. We conclude that the question about the nature of primary sources of UHECRs is directly affected by the assumed temperature redshift relation of the CMB.

Key words: SU(2) Yang-Mills thermodynamics; cosmological model; ultra-high energy cosmic rays, cosmogenic neutrinos

1 INTRODUCTION

The cosmic microwave background (CMB) is the cornerstone of modern Cosmology. Modelling its properties correctly is, however, not only relevant for Cosmology but also vital for the correct description of ultra-high energy cosmic ray (UHECRs) propagation. In this work, we dilute the CMB photon density in comparison to the standard cosmological model Λ CDM, by assuming the so-called SU(2)_{CMB} model (Hofmann 2009; Hahn et al. 2019; Hofmann 2016; Hofmann et al. 2023; Hofmann & Meinert 2023). The purpose of this paper is to discuss how these potential changes to the CMB photon density influence the propagation of UHECRs.

Previous discussions of the consequences of an SU(2)_{CMB} description on UHECR interactions were limited to considering the handedness of the photons, SU(2)_L (Tipler & Piasecki 2018). A fully consistent understanding of the SU(2)_{CMB} model requires applying Yang-Mills thermodynamics and obtaining the modified $T(z)$. Furthermore, the effect of this modified temperature redshift relation on the CMB density produces non-trivial redshift dependences on the UHECR interactions that need to be considered in depth. For a discussion of the impact of modified gravity on UHECR propagation, please see (Sarmah & Goswami 2023). Firstly, the modified $T(z)$ relation is outlined in section 2. The consequences of this relation for all the interactions of UHECRs are discussed in section

3. Section 4 compares fits of UHECRs spectral energy and composition measured by the Pierre Auger Observatory with both U(1) and SU(2) $T(z)$ relations. The corresponding cosmogenic neutrino fluxes are presented in section 5.

2 $T(z)$ RELATION OF SU(2)_{CMB}

In the following, we briefly review the $T(z)$ relation of deconfining SU(2)_{CMB} thermodynamics. For a longer version of the argument, the reader is referred to Hahn & Hofmann (2018); Hofmann & Meinert (2023). The core idea is that the additional degrees of freedom in an SU(2) gauge group lead to the topological constant $1/4^{1/3}$, so that the $T(z)$ relation is for $z \gg 1$ given by

$$T(z)/T_0 = \left(\frac{1}{4}\right)^{1/3} (1+z), \quad (T(z) \gg T(z=0)). \quad (1)$$

To derive this constant, a flat Friedmann-Lemaître-Robertson-Walker (FLRW) universe is assumed:

$$\frac{d\rho}{da} = -\frac{3}{a} (\rho + P), \quad (2)$$

where ρ denotes the energy density, and P the pressure of the deconfined phase in SU(2) thermodynamics. The scale factor a is dimensionless, $a(T(z=0)) = 1$, and related to the redshift z according to $1/a = z + 1$. Eq. (2) has the solution

$$\begin{aligned} a &= \exp\left(-\frac{1}{3} \int_{\rho(T(z=0))}^{\rho(T)} \frac{d\rho}{\rho + P(\rho)}\right) \\ &= \exp\left(-\frac{1}{3} \int_{T(z=0)}^T \underbrace{\frac{1}{T'} \frac{d\rho}{dT'}}_{\kappa} \frac{dT'}{s(T')}\right), \end{aligned} \quad (3)$$

* meinert@uni-wuppertal.de (corresponding author)

† leonel.morejon@uni-wuppertal.de

‡ asandrock@uni-wuppertal.de

§ eiche@tp4.rub.de

¶ jonas.kreidelmeyer@desy.de

|| kampert@uni-wuppertal.de

where the entropy density s is defined as $s = (\rho + P)/T$. By using the Legendre transformation

$$\rho = T \frac{dP}{dT} - P, \quad (4)$$

the term κ can be expressed as

$$\kappa = \frac{1}{T} \frac{d\rho}{dT} = \frac{d^2P}{dT^2} = \frac{ds}{dT}. \quad (5)$$

Substituting Eq. (5) into Eq. (3) finally yields

$$a = \exp\left(-\frac{1}{3} \log \frac{s(T)}{s(T(z=0))}\right). \quad (6)$$

The formal solution (6) is valid for any thermal and conserved fluid subject to expansion in an FLRW universe. If the function $s(T)$ is known, then $T(z)$ can be derived. The ground-state of the deconfining phase is independent of the $T(z)$ relation, since the equation of state for ground-state pressure P^{gs} and energy density ρ^{gs} is $P^{\text{gs}} = -\rho^{\text{gs}}$ (see also Hofmann 2016). Asymptotic freedom occurs nonperturbatively for $T(z) \gg T(z=0)$ (Gross & Wilczek 1973; Politzer 1973; Hofmann 2016), and therefore $s(T)$ is proportional to T^3 . Due to a decoupling of massive vector modes at $T(z=0)$, excitations represent a free photon gas. Therefore, $s(T(z=0))$ is also proportional to $T^3(z=0)$. Correspondingly, the ratio $s(T)/s(T(z=0))$ in Eq. (6) reads

$$\frac{s(T)}{s(T(z=0))} = \frac{g(T)}{g(T(z=0))} \left(\frac{T}{T(z=0)}\right)^3, \quad (T \gg T(z=0)), \quad (7)$$

where g refers to the number of relativistic degrees of freedom at the respective temperatures. SU(2) has one massless gauge mode with two polarisations and two massive gauge modes with three polarisations each, so $g(T) = 2 \times 1 + 3 \times 2 = 8$, for U(1) there is only one massless mode, $g(T(z=0)) = 2 \times 1$. Substituting this into Eq. (7), inserting the result into Eq. (6), and solving for T , one arrives at the high-temperature $T(z)$ relation

$$T(z) = \left(\frac{1}{4}\right)^{1/3} (z+1) T(z=0), \quad (T \gg T(z=0)). \quad (8)$$

Due to two massive vector modes contributing to $s(T)$ at low temperatures, the $T(z)$ relation is modified to

$$T(z) = \mathcal{S}(z)(z+1) T(z=0), \quad (T \geq T(z=0)), \quad (9)$$

where the nonlinear function $\mathcal{S}(z)$ is depicted in Fig. 1 and derived in Hahn et al. (2019). The function $\mathcal{S}(z)$ can be approximated reasonably well with the analytical function

$$\mathcal{S}(z)_{\text{SU}(2)} \approx \exp(-1 - 1.7z) + \left(\frac{1}{4}\right)^{1/3}. \quad (10)$$

This approximation will be used in section 3. However, the numerical solution was applied for all following sections.

3 CHANGES IN PROPAGATION LENGTH

In this section, we discuss the changes to the propagation of ultra-high energy cosmic rays produced by employing the modified temperature relation $T(z)$ from SU(2)_{CMB} as derived in the previous section, Eqs. 8 and 9.

The redshift dependence of the CMB temperature results in scaling and shifting of the differential CMB photon number density $n_{\text{CMB}}(\epsilon, z)$

$$n_{\text{CMB}}(\epsilon, z) = \left(\frac{T(z)}{T_0}\right)^2 n_{\text{CMB}}\left(\epsilon \left(\frac{T(z)}{T_0}\right)^{-1}, 0\right), \quad (11)$$

where ϵ is the energy of the photons, and n_{CMB} as derived from

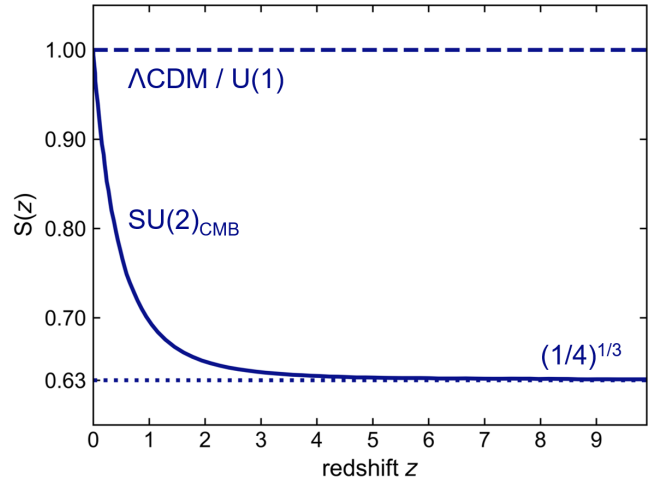


Figure 1: Plot of function $\mathcal{S}(z)$ in Eq. (9) for SU(2)_{CMB} in solid. The conventional $T(z)$ relation of the CMB, as used in the cosmological standard model Λ CDM, associates with the dashed line $\mathcal{S}(z) \equiv 1$. The high-temperature value $1/4^{1/3}$ is approximated by the dotted line $\mathcal{S}(z) = 0.63$.

the Planck distribution is

$$n_{\text{CMB}}(\epsilon, z) = \frac{1}{\pi^2 c^3 \hbar^3} \frac{\epsilon^2}{\exp(\epsilon/k_B T(z)) - 1} \quad (12)$$

where k_B is the Boltzmann constant. The redshift dependence of UHECR interactions with the CMB is reflected in the expression for the energy loss length (Berezinskii et al. 1990)

$$-\frac{1}{E} \frac{dE}{dx} = \int_{\epsilon_0}^{\infty} \frac{k_B T d\epsilon' \sigma(\epsilon') f(\epsilon') \epsilon'}{2\pi^2 \Gamma^2 c^3 \hbar^3} \left\{ -\ln \left[1 - \exp\left(-\frac{\epsilon'}{2\Gamma k_B T}\right) \right] \right\}$$

where E is the energy and $\Gamma = (1 - (v/c)^2)^{-1/2}$ is the Lorentz boost of the UHECRs, and $\sigma(\epsilon')$ is the cross-section for the corresponding interaction (photodisintegration, photomeson, pair-production) and $f(\epsilon')$ is the average inelasticity of the interaction. The scaling of the CMB density produces a corresponding scaling of the interaction rates $\lambda(\Gamma, z)$:

$$\lambda(\Gamma, z) = \left(\frac{T(z)}{T_0}\right)^3 \lambda\left(\frac{T(z)}{T_0} \Gamma, z=0\right). \quad (13)$$

The comparison of the energy loss lengths for U(1) and SU(2) is shown in Fig. 2 (protons) and in Fig. 3 (iron) for $z = 1$. The interaction processes with the CMB are represented separately (photopion, photodisintegration, pair production) while they are grouped into one curve for extragalactic background light (EBL, dotted dark red)¹. For protons at redshift $z = 1$ the energy loss length at the GZK-limit ($E \sim 5 \times 10^{19}$ eV) is shifted by a factor of ~ 2 to higher energies for SU(2) and the propagation lengths for both pair production and photopion production are increased by nearly a factor 3. For iron nuclei at the same redshift, the corresponding photodisintegration limit is also shifted to higher energies by a factor ~ 2 for the SU(2). However, because the energy loss lengths are also increased due to the reduced CMB density, the interactions with the EBL are the dominant ones for cosmic ray energies below 10^{20} eV and therefore the total energy loss length is not increased as much as in the case of protons. This is representative of the case for all intermediate nuclear species with masses between the proton and iron. The increase in energy

¹ In this work we do not include the CMB nor the radio background into the description of the EBL. The EBL remains unchanged under the assumption of an SU(2) gauge group for thermal photons, as the EBL is not thermalized.

loss lengths implies the expansion of the horizon for UHECRs: for protons at all energies, for nuclei at the highest energies starting from about $\sim 10^{19}$ eV. With such an increase, protons from sources at redshift 1 and energies $(1 - 40) \times 10^{19}$ eV would propagate for several hundreds of megaparsecs more than in the case of the U(1), whereas protons at higher energies (where the photopion interactions prevail) would propagate for more than ten megaparsecs.

These increases of propagation horizons are only important when the contribution from distant sources is the dominant one. As the redshift evolves to the present, the U(1) and SU(2)_{CMB} densities converge and by distances of 20 Mpc from Earth the loss lengths differ by only 1.5%. Thus, although protons can propagate further away from sources beyond ~ 200 Mpc in the SU(2) case, they completely lose their energy before reaching our galaxy and only the secondary neutrinos reach us, much like in the U(1) case.

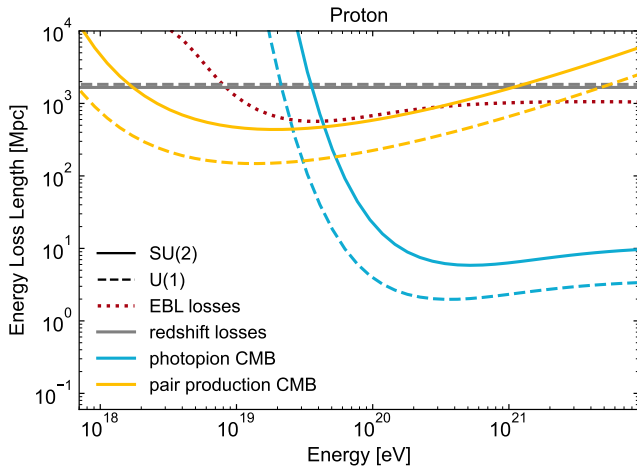


Figure 2: Propagation length of protons at redshift $z = 1$ as a function of the initial particle energy. The normal U(1) and the SU(2) induced $T'(z)$ propagation lengths are shown as dashed and full lines, respectively.

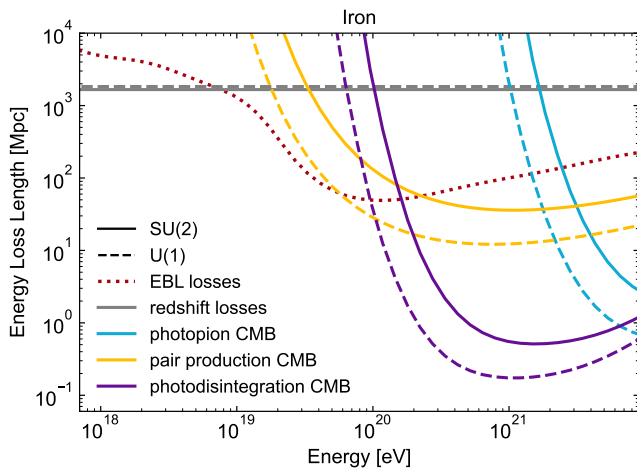


Figure 3: As Fig. 2 for the propagation length of iron nuclei.

Nonetheless, protons coming from sources marginally closer are able to reach our galaxy: at a distance of 200 Mpc Eq. 13 yields a reduction in the interaction rates of $\sim 9\%$ for the SU(2) scenario, see Fig. 2. For nuclei the increased propagation is, however, much less relevant since their propagation lengths are limited to a few dozens of Mpc. For such distances, the reduction in interaction rates with the CMB is of 2 – 4% for SU(2). However, those interactions are overshadowed by the dominant interactions with the EBL.

4 OBSERVATIONAL CONSEQUENCES FOR UHECR ENERGY SPECTRA

We evaluate the impact on the propagation of UHECRs by employing the fit obtained by Heinze et al. (2019) to data from the Pierre Auger Observatory (Aab et al. 2017) under a conventional temperature redshift relation (Λ CDM). The changes in spectral energy and composition produced with the same fit values under SU(2)_{CMB} are obtained by employing the modified $T(z)$ -relation. The propagation of UHECRs was performed using PriNce (Heinze et al. 2019), which is an efficient code to integrate the transport equations for the evolution of cosmic rays at cosmological scales. It includes all the relevant interactions and allows for custom modifications, however, it does not account for the effect of magnetic fields. The propagation scenario considers a population of sources with a continuous distribution in redshift proportional to $(1+z)^m$ with source evolution parameter m obtained from the fit. The sources are assumed to be isotropically distributed and to eject a rigidity-dependent spectral energy flux according to

$$J_A(E) = \mathcal{J}_A f_{\text{cut}}(E, Z_A, R_{\text{max}}) (1+z)^m \left(\frac{E}{E_0}\right)^{-\gamma}, \quad (14)$$

where Z_A is the atomic number and the five nuclear mass groups are indicated by the index A (denoting the nuclear species ^1H , ^4He , ^{14}N , ^{28}Si , and ^{56}Fe). They share the same spectral index γ and the maximal rigidity $R_{\text{max}} = E_{\text{max}}/Z_A$. The cutoff of the injection spectra f_{cut} is defined as

$$f_{\text{cut}}(E) = \begin{cases} 1, & E < Z_A R_{\text{max}} \\ \exp(1 - E/(Z_A R_{\text{max}})), & E > Z_A R_{\text{max}}. \end{cases} \quad (15)$$

\mathcal{J}_A represents the flux of particles of species A emitted per unit of time, comoving volume, and energy. The elemental injection fractions f_A are defined as $f_A = \mathcal{J}_A / (\sum_{A'} \mathcal{J}_{A'})$ at the reference energy $E_0 = 10^{18}$ eV. Here, $\sum_{A'}$ denotes the sum over all chosen nuclear species. Integrating over the injected fluxes J_A leads to the integral fractions of the energy density I_A , which are independent of the choice of E_0 :

$$I_A = \frac{\int_{E_{\text{min}}}^{\infty} J_A E dE}{\sum_{A'} \int_{E_{\text{min}}}^{\infty} J_{A'} E dE} = \frac{\int_{E_{\text{min}}}^{\infty} f_A f_{\text{cut}}(E, Z_A) E^{1-\gamma} dE}{\sum_{A'} \int_{E_{\text{min}}}^{\infty} f_{A'} f_{\text{cut}}(E, Z_{A'}) E^{1-\gamma} dE}, \quad (16)$$

where $E_{\text{min}} = 10^{18}$ eV. For the sake of completeness, we provide both f_A and I_A in the following sections. For SU(2)_{CMB} the following cosmological parameters were used for the propagation: The Hubble parameter $H_0 = 74.24 \text{ km s}^{-1} \text{ Mpc}^{-1}$, a dark energy fraction of $\Omega_\Lambda = 0.616$, and the local matter density $\Omega_{m,0} = 0.384$, compare with Hahn et al. (2019). For U(1)_{CMB} (Λ CDM) the values from the Planck Collaboration were used (Aghanim et al. 2020, p. 15, Table 2), where $H_0 = 67.36 \text{ km s}^{-1} \text{ Mpc}^{-1}$, $\Omega_\Lambda = 0.6847$ and $\Omega_{m,0} = 0.3153$ (TT,TE,EE+lowE+lensing).

The best fit parameters obtained by Heinze et al. (2019) for the conventional Λ CDM relation are reported in Table 1 and plotted in Figure 4 for reference (dashed lines). Fixing these source parameters and propagating the injected UHECR through the SU(2)_{CMB} with its modified $T(z)$ relation yields the solid lines in the same figure. As can be seen, the resulting total flux for SU(2) is virtually unchanged for energies above 6×10^{18} eV, while the fluxes for individual nuclear groups show slightly more pronounced peaks. This effect is a consequence of the modest increase in the horizons. At the same time, the reduction in the pair production losses produces sharper peaks because the effect of energy redistribution corresponding to the U(1) cases is less prominent for SU(2). For protons at the lowest energies, the differences are much more pro-

nounced due to the change in pair production rates as the energies approach 10^{18} eV from above.

EBL	Gilmore et al.	Element	f_A %	I_A %
models	TALYS & Sibyll 2.3c	H	0.0	0.0
redshifts	1 – 0	He	82.0	9.91
γ	-0.8	Ni	17.3	69.99
R_{\max}	1.6×10^{18} V	Si	0.6	16.91
m	4.2	Fe	0.02	3.19

Table 1: Best fit parameters from [Heinze et al. \(2019\)](#), Table 3.

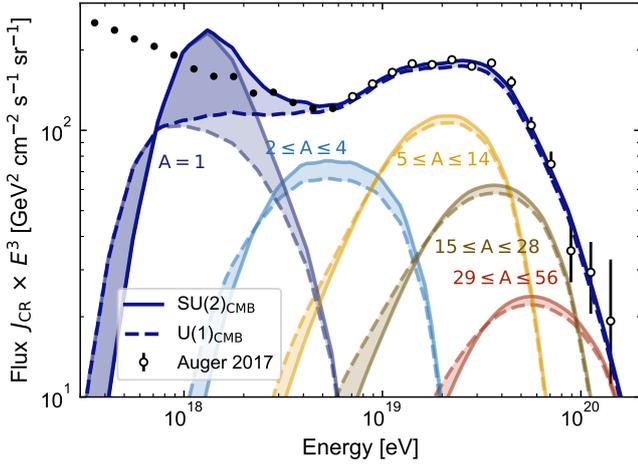


Figure 4: Spectral fit to the 2017 Auger spectral flux data ([Aab et al. 2017](#)) from the best fit parameters in [Heinze et al. \(2019\)](#), see Tab. 1. The fluxes of the normal U(1) and modified SU(2) temperature redshift relations are shown as dashed and full lines, respectively. The χ^2 only considers data points above the ankle region (white dots), as was done in [Heinze et al. \(2019\)](#).

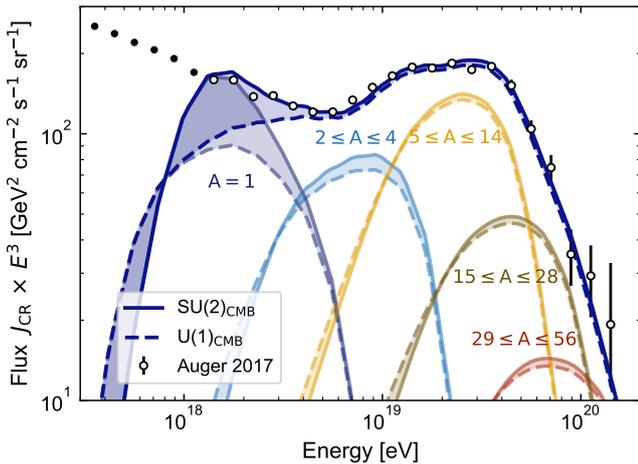


Figure 5: Spectral fit using a gradient descent algorithm to the 2017 Auger spectral flux data, X_{\max} and $\sigma(X_{\max})$ data ([Aab et al. 2017](#)). Here, X_{\max} denotes the position of the shower maximum in the atmosphere. The fluxes of the normal U(1) and modified SU(2) temperature redshift relations are shown as dashed and full lines, respectively. The χ^2 was computed including all the white dots.

Repeating now the combined E , X_{\max} , and $\sigma(X_{\max})$ fit to the same data set of [Aab et al. \(2017\)](#) employing a gradient descent algorithm ([Perrotta 2020](#), p. 33 ff.) for all data points above 1×10^{18} eV in the SU(2)_{CMB} model, we find the best fit parameters shown in Table 2 and plotted in Fig. 5 as full lines. For this fit, the proton excess of SU(2)_{CMB} below the ankle is reduced and the main contributing factor is the shallower source evolution ($m = 2.7$) in contrast to the stronger evolution $m = 4.2$ for U(1) in Heinze’s best fit. The injected chemical composition and the spectral index are only mildly changed, which suggests that the shallower source evolution is enough to compensate for the increased proton horizon and the pileup below the ankle. Note that the proton fraction below the ankle is still too high, in disagreement with the chemical composition inferred from the X_{\max} data (see also appendix B, Fig. 10 c). Below the ankle, an additional galactic component is expected with a heavier composition.

EBL	Gilmore et al.	Element	f_A %	I_A %
models	TALYS & Sibyll 2.3c	H	0.001	0.0
redshifts	1 – 0	He	82.3	9.74
γ	-0.89	Ni	17.4	76.9
R_{\max}	1.74×10^{18} V	Si	0.35	11.6
m	2.7	Fe	0.01	1.72

Table 2: Best fit gradient descent parameters for the SU(2)_{CMB} model.

To better illustrate the SU(2) impact on UHECR propagation, Fig. 6 contrasts the cosmic ray fluxes resulting with a conventional U(1) propagation employing the best fit parameters from Table 2 and scaling the CMB photon density by different factors as shown in the curve labels. The red dotted line in Fig. 6 corresponds to SU(2)_L, where CMB photons interact only with half of the UHECRs due to their handedness.

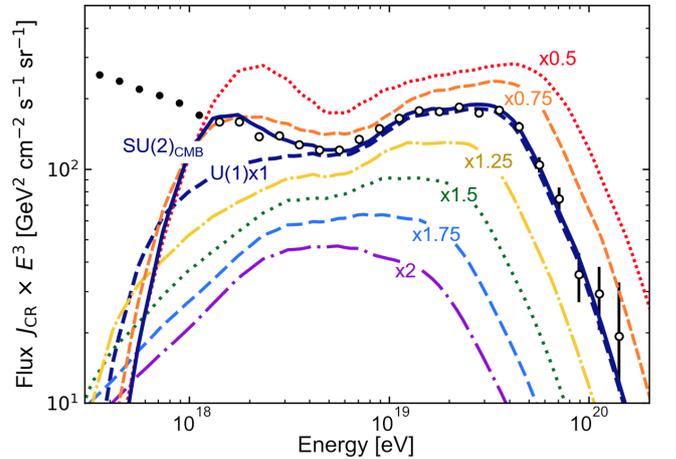


Figure 6: The effect of seven modified CMB photon densities on the total cosmic ray flux is shown in comparison to the normal U(1) temperature redshift relation, as obtained in [Heinze et al. \(2019\)](#) (navy blue, dashed) on top of Auger data from 2017. The best fit parameters of the gradient descent method are used, compare Table 2. The total CR flux for an SU(2) $T(z)$ relation is shown in navy blue. $0.5 \times U(1)$ is shown in red dotted lines, $0.75 \times U(1)$ orange dashed, $1.25 \times U(1)$ yellow dot-dashed, $1.5 \times U(1)$ green dotted, $1.75 \times U(1)$ light blue dashed, $2 \times U(1)$ purple dot-dashed.

The excess in proton flux below the ankle is correlated with the CMB photon density, because these protons come from the disintegration of nuclei. However, this relation is dependent on the

injection spectral index, and it is hard to distinguish an increased proton flux from an additional UHECR source and source evolution. Detailed directional studies which also consider the effects of magnetic fields as well as a better understanding of the chemical composition below the ankle are necessary in order to favour or disfavour the correlation between the slope of the UHECR flux below the ankle and $T(z)$. Note also that only hard spectra, i.e. $\gamma \leq 0$ can increase significantly the UHECR flux below the ankle, because of the larger contribution of the highest energies in secondary protons. Soft injection spectra, e.g. $\gamma \approx 2$ as expected by shock acceleration, do not significantly increase the UHECR flux under $SU(2)_{\text{CMB}}$.

5 COSMOGENIC NEUTRINOS

The expected cosmogenic neutrino fluxes are shown in Fig. 7 for the modified temperature redshift relation under $SU(2)_{\text{CMB}}$ and the normal $T(z)$ for the best fit values from the gradient descent method, Table 2. The neutrino fluxes for $SU(2)_{\text{CMB}}$ peak at slightly higher energies and are slightly increased. The former feature is a consequence of the changed redshift dependence, which increases the energy of the GZK limit in $SU(2)_{\text{CMB}}$ compared to $U(1)$. The latter effect results from the increase in the propagation horizon of the source protons.

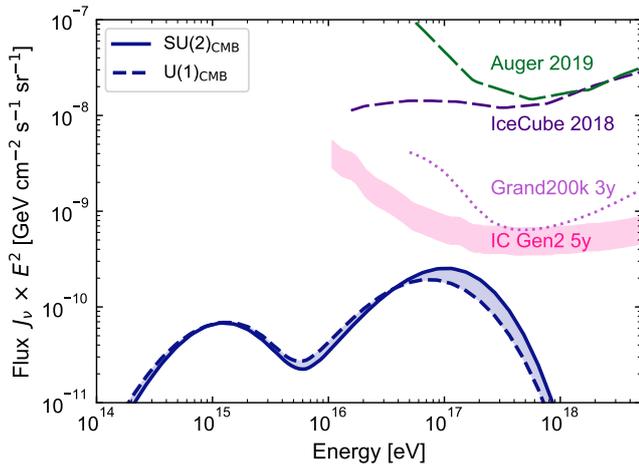


Figure 7: The cosmogenic neutrino flux obtained from the gradient descent fit, Table 2. $SU(2)_{\text{CMB}}$ is shown in navy blue, normal ΛCDM with the corresponding cosmological parameters and $U(1)$ photon propagation is shown in a navy blue dashed line. The pink shaded area represents the projected sensitivity for the IceCube Gen2 radio upgrade after 5 years of observation, compare Fig. 5 in Aartsen et al. (2019). The lavender dotted line indicates the expected sensitivity for Grand200k after 3 years (Álvarez-Muñiz et al. 2020). The dark purple and green dashed lines show 90% CL limits from the IceCube and Pierre Auger Collaboration, respectively (Aartsen et al. 2018; Aab et al. 2019).

Figure 7 shows that changes in the $T(z)$ relation of the CMB only affect the cosmogenic neutrino flux for energies around 10^{17} eV. The peak at around 10^{15} eV, stemming mostly from the decay of neutrons from photodisintegration (see e.g. Ave et al. (2005)) is mostly unaffected except for being slightly narrower due to reduced pair production losses.

In addition to the cosmogenic neutrinos, the photopion production with the CMB also generates γ -rays and the resulting flux at Earth in the case of a $SU(2)_{\text{CMB}}$ would be slightly enhanced compared to the $U(1)_{\text{CMB}}$ due to the increased horizon in the absence of $\gamma\gamma$ -pair production. However, $\gamma\gamma$ -pair production and inverse Compton

scattering with the EBL are the dominant interactions, in particular for γ -ray energies ≤ 100 TeV, therefore, after the cascading of photon we expect no significant difference in the cosmogenic γ -ray flux between the $SU(2)_{\text{CMB}}$ and the $U(1)_{\text{CMB}}$.

6 SUMMARY AND OUTLOOK

In this paper, we examined the impact of locally non-linear modification of the CMB temperature redshift relation $T(z)$ on the fit to ultra-high energy cosmic rays and the corresponding cosmogenic neutrinos.

The reduction of the CMB densities is found to affect significantly the interaction lengths of UHECRs with CMB photons in the redshift range of relevance for UHECR propagation, resulting in extended horizons for protons and UHECR nuclei. However, the increase in interaction lengths has only a modest effect on the observed UHECR flux due to interactions with the EBL, which then become dominant for the energies of relevance. Hence, a comparison to an existing fit of UHECRs yields similar flux of UHECRs nuclei but differs considerably for protons where a pronounced bump appears below the ankle for the $SU(2)_{\text{CMB}}$ for hard injection spectra.

In order not to exceed the total UHECR flux and to agree with Auger data in the case of a hard injection spectrum, a shallower source evolution of cosmic ray sources of $m \approx 2.7$ is needed, which is more in line with SGBs and GRBs than with AGNs. This is in agreement with recent studies that consider arrival directions and extragalactic magnetic fields for energies beyond the ankle ($\geq 5 \times 10^{18}$ eV) (Bister 2023).

While the confirmation of the $SU(2)_{\text{CMB}}$ description requires further studies, the present work provides constraints for its validity. The independent determination of the redshift evolution of UHECR sources has the potential to reject the $SU(2)_{\text{CMB}}$ temperature redshift relation for *hard* injection spectra: for a steeper cosmic ray source evolution, the predicted proton contribution below the ankle would be in tension with observations.

Since there is currently no firm preference for a specific UHECR source class (Abreu et al. 2022), we would like to add modified $T(z)$ and in particular in the case of $SU(2)_{\text{CMB}}$ to the discussion. This adds another tool to discriminate potential source classes and vice versa, constraining the sources by other means while simultaneously improving the knowledge of the UHECR composition may lead to a direct probe of $T(z)$ of the CMB in the future.

7 DATA AVAILABILITY

The simulation scripts used in this study are available upon request, and the authors welcome inquiries for collaboration.

8 ACKNOWLEDGEMENTS

JM acknowledges insightful discussions with Ralf Hofmann and Wolfgang Rhode.

This work is supported by SFB 1491 (Project A3) and partially by the Vector Foundation under grant number P2021-0102. LM's work is supported by the DFG under grant number 445990517 (KA 710).

REFERENCES

- Aab A., et al., 2017, *J. Cosmol. Astropart. Phys.*, 04, 038
- Aab A., et al., 2019, *J. Cosmol. Astropart. Phys.*, 10, 022
- Aartsen M. G., et al., 2018, *Phys. Rev. D*, 98, 062003
- Aartsen M. G., et al., 2019, Neutrino astronomy with the next generation IceCube Neutrino Observatory ([arXiv:1911.02561](https://arxiv.org/abs/1911.02561))
- Abreu P., et al., 2022, *Astrophys. J.*, 935, 170
- Aghanim N., et al., 2020, *Astron. Astrophys.*, 641, A6
- Álvarez-Muñiz J., et al., 2020, *Sci. China Phys. Mech. Astron.*, 63, 219501
- Ave M., Busca N., Olinto A. V., Watson A. A., Yamamoto T., 2005, *Astropart. Phys.*, 23, 19
- Bellido J., 2018, *PoS, ICRC2017*, 506
- Berezinskii V. S., Bulanov S. V., Dogiel V. A., Ptuskin V. S., 1990, *Astrophysics of cosmic rays*. North-Holland, Amsterdam
- Bister T., 2023, *EPJ Web Conf.*, 283, 03008
- Gross D. J., Wilczek F., 1973, *Phys. Rev. Lett.*, 30, 1343
- Hahn S., Hofmann R., 2018, *Mod. Phys. Lett. A*, 2016, 1850029
- Hahn S., Hofmann R., Kramer D., 2019, *Mon. Not. Roy. Astron. Soc.*, 482, 4290
- Heinze J., Fedynitch A., Boncioli D., Winter W., 2019, *Astrophys. J.*, 873, 88
- Hofmann R., 2009, *Annalen Phys. (Berlin)*, 18, 634
- Hofmann R., 2016, *The thermodynamics of quantum Yang-Mills theory: Theory and applications*, 2nd edition. World Scientific
- Hofmann R., Meinert J., 2023, *Astronomy*, 2, 286
- Hofmann R., Meinert J., Balaji S. S., 2023, *Annalen Phys.*, 535, 2200517
- Ostapchenko S., 2011, *Phys. Rev. D*, 83, 014018
- Perrotta P., 2020, *Programming Machine Learning: From Coding to Deep Learning*, 1st edition. Pragmatic Bookshelf
- Pierog T., Karpenko I., Katzy J. M., Yatsenko E., Werner K., 2015, *Phys. Rev. C*, 92, 034906
- Politzer H. D., 1973, *Phys. Rev. Lett.*, 30, 1346
- Riehn F., Engel R., Fedynitch A., Gaisser T. K., Stanev T., 2016, *PoS, ICRC2015*, 558
- Sarmah S. P., Goswami U. D., 2023, *Propagation and Fluxes of Ultra High Energy Cosmic Rays in f(R) Gravity Theory* ([arXiv:2303.16678](https://arxiv.org/abs/2303.16678))
- Tipler F. J., Piasecki D. W., 2018, *Using UHE Cosmic Rays to Probe the CBR and Test Standard Model Particle Physics* ([arXiv:1809.08492](https://arxiv.org/abs/1809.08492))

APPENDIX A: BEST FIT HEINZE SU(2)_{CMB}

The best fit from [Heinze et al. \(2019\)](#) is reproduced in Fig. 9 a) alongside the cosmogenic neutrino flux, Fig. 9 b), the X_{\max} data Fig. 9 c) and $\sigma(X_{\max})$ data, Fig. 9 d) overlaid by three hadronic interaction models.

All χ^2 for the X_{\max} of the best fit in Fig. 9 c) and the χ^2 for $\sigma(X_{\max})$ of the best fit in Fig. 9 d) are shown in table 3.

reduced χ^2 for	X_{\max} in Fig. 9 c)		$\sigma(X_{\max})$ in Fig. 9 d)	
Model	U(1)	SU(2) _{CMB}	U(1)	SU(2) _{CMB}
EPOS-LHC	2.21	2.2	11.76	10.96
Sibyll 2.3 c	0.91	1.36	4.02	4.25
QGSJET-II.04	5.39	4.79	3.64	3.75

Table 3: The reduced χ^2 for the $\sigma(X_{\max})$ of the best fit in Fig. 10 d). Seven degrees of freedom were assumed.

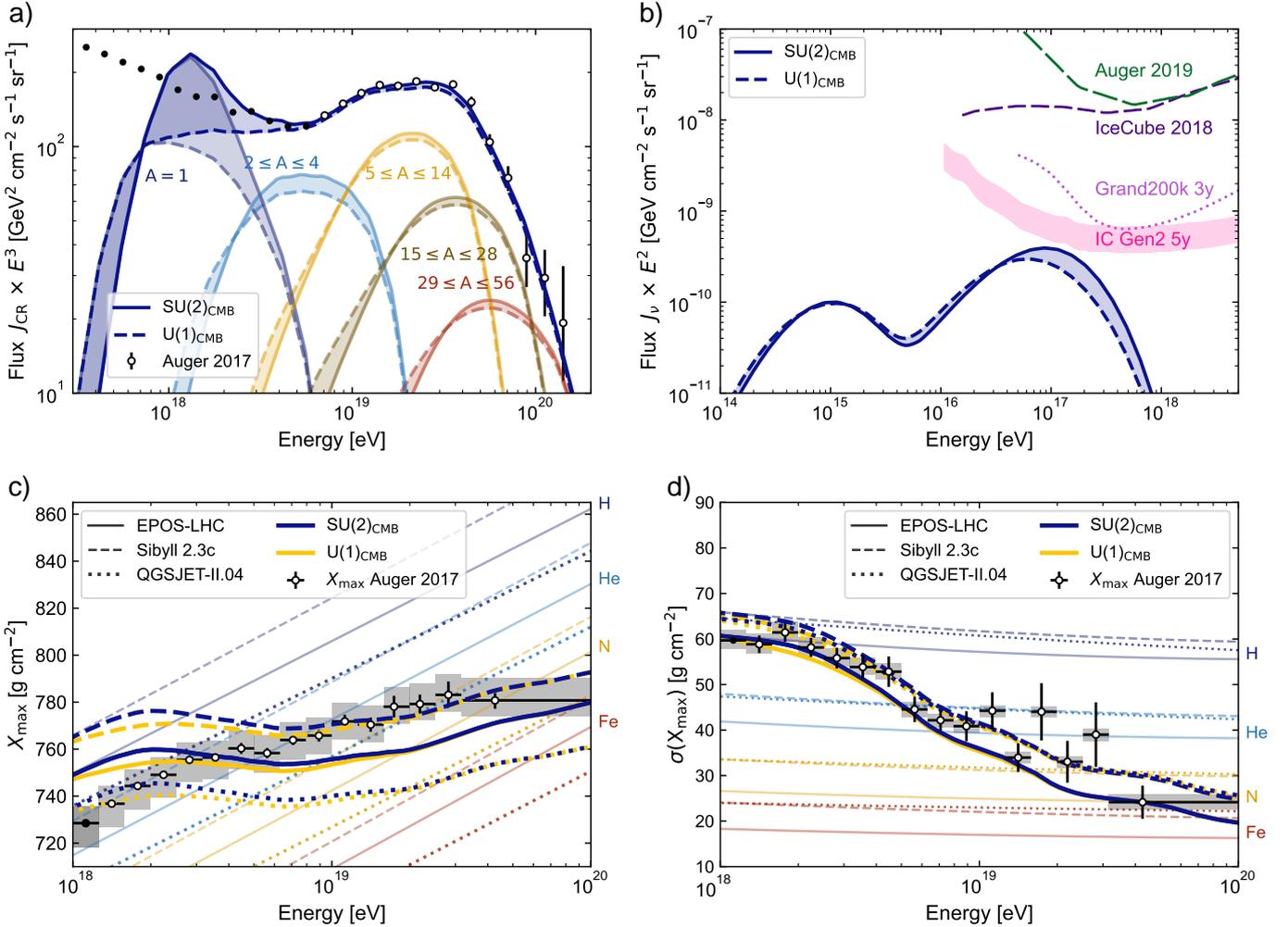


Figure 9: **a)** Spectral fit to the 2017 Auger spectral flux data from the best fit parameters in [Heinze et al. \(2019\)](#), see Tab. 1. [Heinze et al. \(2019\)](#) assume a normal U(1) temperature redshift relation (dashed lines, total flux dashed navy blue). The total cosmic ray flux with an SU(2) temperature redshift relation is shown with a blue solid line. The χ^2 only consider data points including the ankle region (white dots), according to [Heinze's choice](#). **b)** The cosmogenic neutrino flux obtained from the fit in (a) in SU(2)_{CMB} is shown in navy blue solid, [Heinze et al. \(2019\)](#) in navy blue dashed lines. The pink shaded area represents the projected sensitivity for the IceCube Gen2 radio upgrade after 5 years of observation, compare Fig. 5 in [Aartsen et al. \(2019\)](#). The lavender dotted line indicates the expected sensitivity for Grand200k after 3 years [Álvarez-Muñiz et al. \(2020\)](#). The dark purple dashed line shows 90% CL limits from the IceCube Collaboration (2018) ([Aartsen et al. 2018](#)). And the green dashes line represents the 90% CL limit from the Pierre Auger Collaboration (2019) ([Aab et al. 2019](#)). **c)** The Auger 2017 $\langle X_{\max} \rangle$ and **d)** $\sigma(X_{\max})$ data ([Bellido 2018](#)), on top of three different air-shower model expectations: Epos-LHC ([Pierog et al. 2015](#)) (solid lines), Sibyll 2.3c ([Riehn et al. 2016](#)) (dashed bold lines) and QGSJET-II.04 ([Ostapchenko 2011](#)) (dotted lines). For calculating the relative χ^2 the same energy ranges as in Fig. 10 c) and d) have been chosen for better compatibility.

APPENDIX B: BEST FIT SU(2)_{CMB}

In order to mitigate the proton excess below the ankle in the reproduced model from [Heinze et al. \(2019\)](#), a descending algorithm is used. It minimizes the χ^2 for the white spectral data points in Fig. 10 a), X_{\max} in Fig. 10 c) and $\sigma(X_{\max})$ in Fig. 10 d). The best fit parameter to the Pierre Auger Collaboration data from 2017 are shown in Table 2.

All χ^2 for the X_{\max} of the best fit in Fig. 10 c) and the χ^2 for $\sigma(X_{\max})$ of the fit in Fig. 10 d) are given in table 4.

Model	X_{\max} in Fig. 10 c)		$\sigma(X_{\max})$ in Fig. 10 d)	
	U(1)	SU(2) _{CMB}	U(1)	SU(2) _{CMB}
EPOS-LHC	0.98	1.01	8.97	8.53
Sibyll 2.3 c	1.57	2.0	4.86	5.18
QGSJET-II.04	3.76	3.45	4.11	4.36

Table 4: The reduced χ^2 for the $\sigma(X_{\max})$ of the fit in Fig 10 d). Seven degrees of freedom were assumed.

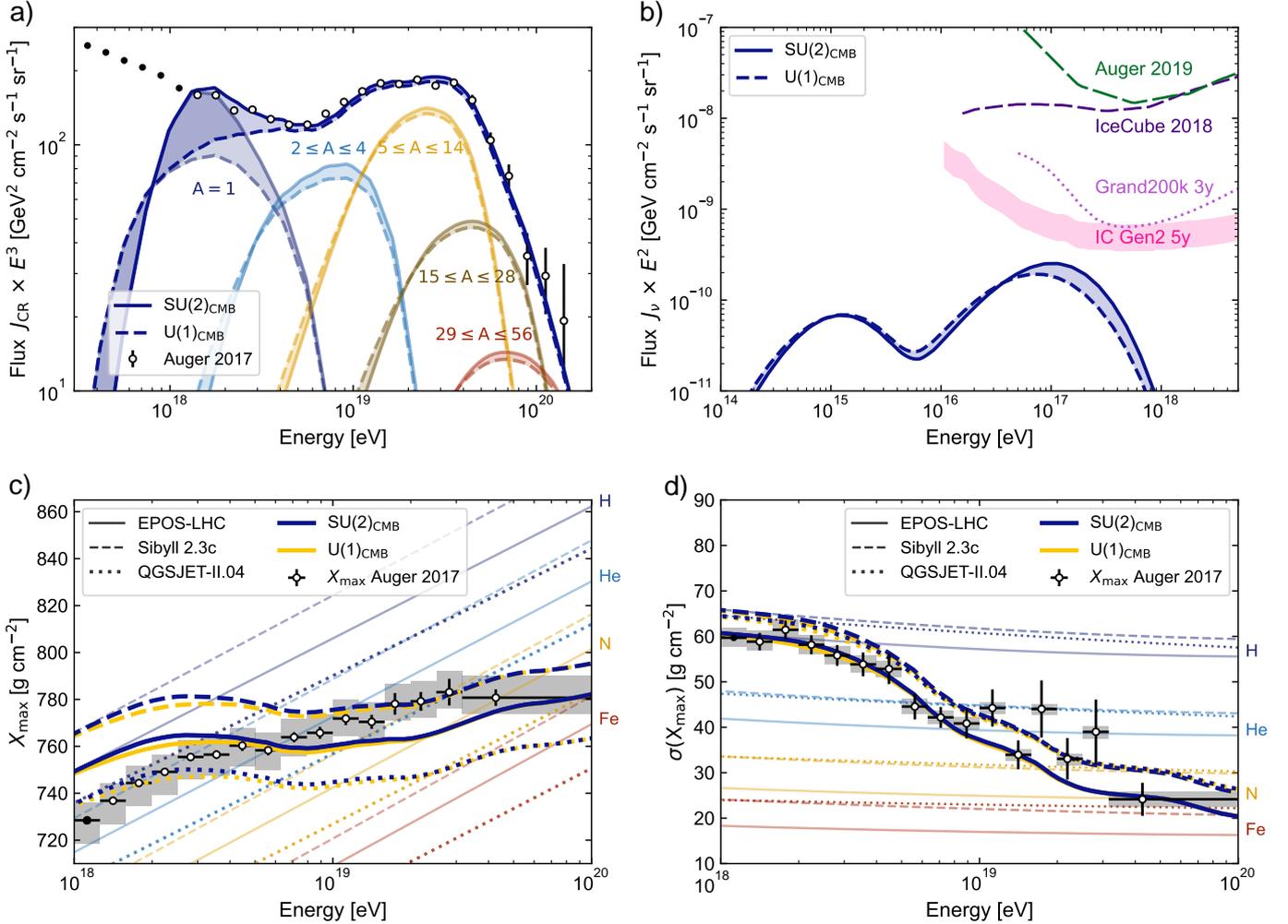


Figure 10: **a)** Spectral fit to the 2017 Auger spectral flux data from the best fit parameters in [Heinze et al. \(2019\)](#), see Tab. 1. [Heinze et al. \(2019\)](#) assume a normal U(1) temperature redshift relation (dashed lines, total flux dashed navy blue). The total cosmic ray flux with an SU(2) temperature redshift relation is shown with a blue solid line. The χ^2 only consider data points including the ankle region (white dots), according to Heinze's choice. **b)** The cosmogenic neutrino flux obtained from the fit in (a) in SU(2)_{CMB} is shown in navy blue solid, ([Heinze et al. 2019](#)) in navy blue dashed lines. The pink shaded area represents the projected sensitivity for the IceCube Gen2 radio upgrade after 5 years of observation, compare Fig. 5 in [Aartsen et al. \(2019\)](#). The lavender dotted line indicates the expected sensitivity for Grand200k after 3 years [Álvarez-Muñiz et al. \(2020\)](#). The dark purple dashed line shows 90% CL limits from the IceCube Collaboration (2018) ([Aartsen et al. 2018](#)), and the green dashes line represents the 90% CL limit from the Pierre Auger Collaboration (2019) ([Aab et al. 2019](#)). **c)** The Auger 2017 $\langle X_{\max} \rangle$ and **d)** $\sigma(X_{\max})$ data ([Bellido 2018](#)), on top of three different air-shower model expectations: Epos-LHC ([Pierog et al. 2015](#)) (solid lines), Sibyll 2.3c ([Riehn et al. 2016](#)) (dashed bold lines) and QGSJET-II.04 ([Ostapchenko 2011](#)) (dotted lines).